

Title: Altermagnetic Polar Metallic phase in Ultra-Thin Epitaxially-Strained RuO₂ Films

Authors: Seung Gyo Jeong^{1,†,*}, In Hyeok Choi^{2,†,*}, Sreejith Nair¹, Luca Buiarelli¹, Bitu Pourbahari^{3,4}, Jin Young Oh⁵, Nabil Bassim^{3,4}, Ambrose Seo⁶, Woo Seok Choi⁴, Rafael M. Fernandes⁷, Turan Birol¹, Liuyan Zhao⁸, Jong Seok Lee^{2,*}, and Bharat Jalan^{1,*}

Affiliations:

¹Department of Chemical Engineering and Materials Science, University of Minnesota–Twin Cities, Minneapolis, Minnesota 55455, United States

²Department of Physics and Photon Science, Gwangju Institute of Science and Technology (GIST), Gwangju 61005, Republic of Korea

³Canadian Centre for Electron Microscopy and Department of Materials Science and Engineering, McMaster University, Hamilton, ON L8S 4L8, Canada

⁴Department of Materials Science and Engineering, McMaster University, Hamilton L8S 1L9, Canada

⁵Department of Physics, Sungkyunkwan University, Suwon 16419, Republic of Korea

⁶Department of Physics and Astronomy, University of Kentucky, Lexington, Kentucky 40506, United States

⁷School of Physics and Astronomy, University of Minnesota–Twin Cities, Minneapolis, Minnesota 55455, United States

⁸Department of Physics, University of Michigan, 450 Church Street, Ann Arbor, Michigan 48109, United States

*Corresponding authors. Email: jeong397@umn.edu, jys2316@gm.gist.ac.kr, jsl@gist.ac.kr, bjalan@umn.edu

†These authors contributed equally to this work

Abstract: Altermagnetism refers to a wide class of compensated magnetic orders featuring magnetic sublattices with opposite spins related by rotational symmetry rather than inversion or translational operations, resulting in non-trivial spin splitting and high-order multipolar orders. Here, by combining theoretical analysis, electrical transport, X-ray and optical spectroscopies, and nonlinear optical measurements, we establish a phase diagram in hybrid molecular beam epitaxy-grown RuO₂/TiO₂ (110) films, mapping the broken symmetries along the altermagnetic/electronic/structural phase transitions as functions of film thickness and temperature. This phase diagram features a novel altermagnetic metallic polar phase in strained 2 nm samples, extending the concept of multiferroics to altermagnetic systems. These results provide a comprehensive understanding of altermagnetism upon epitaxial heterostructure design for emergent novel phases with multifunctionalities.

One-Sentence Summary: Comprehensive study of altermagnetic phase diagram reveals a novel altermagnetic polar metallic phase in epitaxial RuO₂ thin films.

Main Text: Magnetic order, i.e. self-organization of magnetic moments of electrons in a solid, necessarily breaks the time-reversal symmetry and possibly the translational, inversion, and/or rotational symmetries (1, 2). These broken symmetries govern both the occurrence and the nature of the spin-splitting in the electronic band structure (1, 3). In non-compensated magnetic systems characterized by broken time-reversal symmetry, such as ferromagnets, the Zeeman coupling induces a conventional exchange spin-splitting throughout the Brillouin zone. In conventional collinear compensated antiferromagnets, because time-reversal (TR) combined with a translation or an inversion is a symmetry of the systems, no spin-splitting emerges. Surprisingly and interestingly, in altermagnets – a newly introduced type of collinear compensated magnets that are invariant under the combination of TR and rotation (2, 4), nonzero higher rank multipoles in the momentum space arise in the absence of net magnetic dipole moment (5, 6). While various even-parity TR-odd multipoles are possible, a common example is the case of magnetic octupoles, which induce a *d*-wave momentum-dependent spin-splitting in the electronic bands (4, 7). This novel magnetic phase has garnered significant attention in recent studies and is found in systems with symmetries distinct from those of antiferromagnets (1, 2, 4-6, 8-15). To probe the theoretically predicted altermagnetic order parameters, comprehensive characterization of the electronic, structural, and magnetic properties is essential. To date, experimental observations of altermagnetism have often relied on electrical transport with magnetic field and angle-resolved photoemission spectroscopy at low-temperature (16-23), which attests to the challenges of directly detecting the altermagnetic order parameter and coupled structural and magnetic symmetries across transition temperature.

Rutile RuO₂ is an altermagnetic candidate with non-relativistic spin splitting characterized by a nonzero magnetic octupole moment in momentum space and vanishing lower-order magnetic multipoles (2, 16, 24). Recent studies employing synchrotron X-ray and neutron diffractions have identified itinerant antiferromagnetic order in RuO₂ (25-27), encouraging further investigation of the symmetries of its magnetic order. Bulk RuO₂ has the tetragonal $4/mmm$ structural and is expected to exhibit $4'/mmm'$ magnetic point group (space groups $P4_2/mnm$ and $P4'_2/mnm'$, respectively) (1), where the magnetic moments are along the [001] axis. The altermagnetic phase of RuO₂ is reported to introduce many spin-related functionalities, including the anomalous Hall effect depending on the magnetic field orientation, thermal Hall effect, large tunneling magnetoresistance, and magneto-optical effects (1, 4, 17, 28-30). Despite its significance to both fundamental understanding and potential spintronic applications, a comprehensive experimental characterization of the altermagnetic phase diagram has not been reported yet in RuO₂ (16, 17).

In this study, we investigated the altermagnetic order parameter in RuO₂ and its dependence on the crystal symmetry, down to the nano-scale limit. Epitaxial strain engineering serves as an accessible means for manipulating crystal symmetry (31-33), allowing us to explore the relationship between structural symmetry and the altermagnetic order parameter. Here, crystal symmetry manipulation of RuO₂ was achieved through epitaxial RuO₂/TiO₂ (110) heterostructures grown using hybrid molecular beam epitaxy (MBE) (34, 35), as described in the Method section. The crystal symmetry and coupled altermagnetic order parameters were characterized by symmetry-sensitive optical second harmonic generation (SHG), depicted schematically in Fig. 1. The SHG signal is known to display both the TR-even structural and TR-odd magnetic contributions, as well as their coherent interference in magnetic systems (36-39). By tracking the SHG signal across the altermagnetic transition temperature (T_c), the detected TR-odd contribution in SHG directly probes the altermagnetic order parameter, and the corresponding magnetic octupolar order. By combining SHG with group theory, density functional theory calculations, electrical transport, X-ray absorption spectroscopy, and optical spectroscopy, we established a

comprehensive phase diagram for epitaxial RuO₂, depicting crystal symmetry, electronic properties, and altermagnetic transition as functions of thickness and temperature. Notably, we discovered a novel altermagnetic polar metallic phase in an epitaxially strained RuO₂ film of thickness 2 nm. Our study paves the way to understanding altermagnetic order parameters and the controllability of correlated orders through the deliberate epitaxial design of heterostructures.

We first discuss the crystal structure of RuO₂/TiO₂ (110) films as a function of film thickness (t). All RuO₂ films have atomically flat surfaces confirmed by both atomic force microscopy and X-ray reflectivity measurements (Fig. S1). Fig. 2A shows a schematic representation of strained RuO₂/TiO₂ (110) film (left panel) and bulk RuO₂ (right panel) along the [001] direction, where the lattice mismatches between RuO₂ and TiO₂ are -4.7% (along [001]) and $+2.3\%$ (along [1 $\bar{1}$ 0]) (35, 40). This anisotropic strain breaks the tetragonal symmetry of RuO₂ and reduces the space group to $Cmmm$, which can be further reduced to polar $Amm2$ due to interface effects in thin films (Fig. S2). Fig. 2B shows X-ray diffraction (XRD) reciprocal space maps (RSMs) of 4 and 17 nm RuO₂ films measured at the (310) Bragg diffraction of TiO₂ substrate. For the 4 nm film (left panel), a narrow tail signal of strained RuO₂ is observed along the [110] direction, whereas for the 17 nm film (right panel), a wider peak towards bulk RuO₂ is observed, indicative of partial strain relaxation (35). Although the RuO₂ lattice along [1 $\bar{1}$ 0] is nearly fully strained in the 4 nm film, and slightly relaxed in the 17 nm film, RSMs at the (332) Bragg diffraction of TiO₂ (Fig. S3) reveal significant strain relaxation along [001] for $t \geq 6$ nm. The high-angle annular dark-field scanning transmission electron microscopy (HAADF-STEM) of an 11 nm RuO₂ film reveals local structural dislocations along the [001] direction only, indicating strain relaxation consistent with the XRD results (Fig. S4). For $t \leq 4$ nm, the film peak intensity weakens, making it difficult to distinguish between the peaks of the RuO₂ film and the TiO₂ substrate in RSMs. These results suggest that the onset of strain relaxation begins at film thickness as small as 6 nm.

To further investigate the full symmetries of these films, we performed rotational anisotropy (RA) SHG measurements at an oblique incident angle $\theta = 45^\circ$, where the SHG intensity is recorded as a function of the azimuthal angle φ between the light scattering plane and the in-plane crystal axis [1 $\bar{1}$ 0] (Fig. 1). The incidence fundamental and the reflected outgoing SHG light polarization can be chosen to be either parallel (P) or normal (S) to the light scattering plane, resulting in a total of four polarization channels, P/S_{in}-P/S_{out} (equivalently PP, PS, SP, and SS). The RA SHG data is typically presented in polar plots to better visualize the symmetries. We first examine in Fig. 2C the thickness-dependent evolution of SHG polar plots in the PP ($I_{\text{SHG}}^{\text{PP}}(\varphi)$, upper panels) and SS configurations ($I_{\text{SHG}}^{\text{SS}}(\varphi)$, lower panels) at $\theta = 45^\circ$. These measurements were performed at 560 K (above the predicted $T_c = 400$ K corresponding to magnetic order, (I)) for the crystalline symmetry characterization by avoiding any potential contribution from the altermagnetic order. We observe that the RA SHG patterns evolve dramatically with a variation of t , with abrupt changes for $t \geq 4$ nm. In Fig. 2D, we plot the angularly averaged SHG field strength in the PP and SS configurations

as a function of t , i.e., $\sqrt{I_{\text{SHG}}^{\text{PP or SS}}(t)} = \sqrt{\frac{1}{2\pi} \int_0^{2\pi} I_{\text{SHG}}^{\text{PP or SS}}(\varphi, t) d\varphi}$. $\sqrt{I_{\text{SHG}}^{\text{PP}}(t)}$ exhibits a t -dependent enhancement with significantly different slopes for films with $t \leq 2$ nm and $t \geq 4$ nm. These results of RA SHG suggest a structural phase transition in RuO₂ occurring at $2 \text{ nm} \leq t \leq 4 \text{ nm}$. Consistent with this finding, we observe a dramatic change in the crystal field energy and Hall coefficients in X-ray absorption spectroscopy and electrical Hall transports, respectively (see Fig. S5). A similar critical thickness was recently reported in the crystallographic anisotropy of the electrical transport in RuO₂/TiO₂ (110) (41) and attributed to the anisotropic strain relaxation in RuO₂/TiO₂ (110).

Detailed analyses of the experimentally observed RA SHG patterns revealed the crystalline symmetries of each thickness range. For strained RuO₂ films when $t \leq 2$ nm, $I_{\text{SHG}}^{\text{SS}}$ is negligible while the other polarization configurations give non-zero and symmetric SHG responses. As an example of the 2 nm RuO₂ film, Fig. S6 shows that RA SHG in the PP, SP, and PS configuration exhibit a 2-fold rotational axis about the [110] axis and two mirrors normal to the $[\bar{1}\bar{1}0]$ and [001] directions (bottom panel of Fig. 2E). This in combination with the absence of SHG in the SS channel leads to the identification of the electric dipole (ED, blue lines in Fig. 2C) contribution to SHG under the non-centrosymmetric $mm2$ point group for $t \leq 2$ nm, revealing the breaking of the mirror perpendicular to the [110] axis (Supplementary Text S1, Table S1, and Fig. S6, S7, and S8). The oblique incident angle θ -dependence of I_{SHG} further supports the conclusion that the structural symmetry for $t \leq 2$ nm is that of the $mm2$ point group (Supplementary Text S2 and Fig. S9). Furthermore, for $t \leq 2$ nm, the increase of I_{SHG} with increasing t suggests that the ED SHG is a bulk response throughout the whole film thickness. It is noteworthy that according to group theory, the combination of strain and/or magnetic order cannot give rise to the $mm2$ point group (or any of its magnetic invariants) for thin (≤ 2 nm) RuO₂ (110) film (Fig. S2). Instead, this point group $mm2$ can be obtained by considering the bulk point group $4/mmm$ in the presence of an electric polarization along [110]. Hence, the polar, non-centrosymmetric point group $mm2$ identified in our SHG measurements is a result of either an intrinsic polar symmetry breaking in RuO₂, or an interface effect, which is equivalent to the emergence of a polarization in the [110] direction. While density functional theory (DFT) calculations predict lattice instabilities at the zone-boundary in the strained RuO₂ (42), there are no reported zone-center instabilities, suggesting that strain alone cannot induce a polar structure. It is possible, however, that the polar field on the interface stabilizes a polar phase throughout the strained thin films, and hence, the inversion symmetry breaking along the out-of-plane [110] axis can be present in the whole RuO₂ films for $t \leq 2$ nm, as schematically illustrated in the top panel of Fig. 2E. Meanwhile, in strain-relaxed films ($t \geq 4$ nm), the RA SHG patterns could be well explained (black and grey lines in Fig. 2C) by considering the electric quadrupole (EQ) contribution of the non-polar, centrosymmetric point group $4/mmm$ consistent with the structural symmetry of bulk RuO₂. Both $I_{\text{SHG}}^{\text{PP}}$ and $I_{\text{SHG}}^{\text{SS}}$ exhibit a linear t -dependence for $t \geq 4$ nm suggesting the bulk origin of $4/mmm$ EQ SHG, rather than the interfacial contribution.

Now we turn to the discussion of the temperature-dependent RA SHG which, as we will argue, shows the time-reversal symmetry breaking in both strained and relaxed RuO₂ films below $T_c \sim 510$ K (Fig. 3A-3C). Fig. 3A shows a comparison of $I_{\text{SHG}}^{\text{PP or SS}}(\varphi)$ below T_c (320 and 420 K) and above T_c (540 K) for the 2 nm (upper panel) and 17 nm (lower panel) RuO₂ films. In the strained 2 nm film, the anisotropy of the $I_{\text{SHG}}^{\text{PP}}(\varphi)$ patterns shows a significant temperature-dependence accompanied by a large enhancement of the signal amplitude, whereas $I_{\text{SHG}}^{\text{SS}}$ shows no temperature-dependence and remains below the noise level (Fig. S10). In Fig. 3B, the second-order susceptibility tensor $\chi_{\text{PP}}^{\text{ED}}$ (blue circles) at $\varphi = 90^\circ$ obtained from $I_{\text{SHG}}^{\text{PP}}$ also exhibits an anomaly around 510 K. As there is no discernible change in the linear reflectivity $R^{1\omega}$ (grey circles), the observed change in $I_{\text{SHG}}^{\text{PP}}(\varphi)$ can be attributed solely to nonlinear optical response possibly reflecting the magnetic transition. Notably, while $I_{\text{SHG}}^{\text{PP}}(\varphi)$ at 540 K is mirror-symmetric for $\varphi = 0^\circ$ along $[\bar{1}\bar{1}0]$ and 90° along [001] (dotted lines) that is consistent with the structural point group $mm2$, the 2-fold symmetric $I_{\text{SHG}}^{\text{PP}}(\varphi)$ data at 320 K and 420 K shows two clear dips at $\varphi = 60^\circ$ and 240° (marked by the arrows) that are not present at $\varphi = 120^\circ$ and 300° (Fig. 3A and 3D). Therefore, this reveals the magnetism in the strained 2 nm RuO₂ films breaks two mirrors normal to the $[\bar{1}\bar{1}0]$

and [001] directions and retains the 2-fold rotational axis along [110]. The highest magnetic subgroup of $mm2.1'$ is $m'm'2$, with magnetic moments along [110] in an altermagnetic configuration (upper panel of Fig. 3E). The $m'm'2$ magnetic point group can produce both time-invariant (i -type) and time-variant (c -type) ED SHG that scale with the even and odd powers of the magnetic order parameter, respectively. The RA SHG of the 2 nm film at 320 K and 420K is well fit by the coherent interference between the i -type magnetic ED SHG of $m'm'2$ (or equivalently, structural ED SHG of $mm2$) and c -type magnetic ED SHG of $m'm'2$, as shown in Fig. 3A and by the blue line in Fig. 3D. On the other hand, if we had assumed magnetic moments along [001] as expected in the altermagnetic bulk phase (lower panel in Fig. 3E), we would have obtained the subgroup $m'm2'$. However, $m'm2'$ dictates the presence of the mirror normal to [001], which is absent in our RA SHG data, and the absence of the 2-fold rotational axis along [110], which is nevertheless present in the RA SHG. Hence, the interference between this c -type ED SHG under $m'm2'$ and the structural ED SHG under $mm2$ cannot fit $I_{\text{SHG}}^{\text{PP}}(\varphi)$ at 320 K (green curve in Fig. 3D). Furthermore, the absence of a $I_{\text{SHG}}^{\text{SS}}(\varphi)$ signal also supports the conclusion that the magnetic point group is $m'm'2$ rather than $m'm2'$ for the strained films (Supplementary Text S1). To achieve the $m'm'2$ magnetic point group, there must be a rotation of the magnetic moments from the [001] (which is the expected orientation at bulk) in-plane direction to the [110] out-of-plane direction. Such a rotation was previously proposed to be partially achieved via a magnetic field (4, 17); our experiments show that it can be completely realized by epitaxial strain. Since an out-of-plane magnetic easy axis contradicts the typical expectation from thin film geometry, which usually favors an in-plane easy axis, this rotation is likely attributed to the modification of the crystal field (and consequently the orbital angular momentum) on the Ru ion.

Interestingly, both $m'm2'$ and $m'm'2$ phases allow a weak-ferromagnetic moment, which is distinct from bulk RuO₂. Fig. 3F shows the non-collinear spin density of RuO₂ for both cases for [110] and [001] spin components ($S_{[110]}$ and $S_{[001]}$) calculated by DFT (see Methods for more detail). The primary component, which is parallel to the magnetic moment orientation, when integrated, gives a nonzero magnetic moment ($\sim 0.01 \mu_{\text{B}}$); in other words, strained RuO₂ is no longer a compensated antiferromagnet when spin-orbit coupling is considered. This is a straightforward consequence of the general piezomagnetic properties of altermagnets (6). It is interesting to note that Dzyaloshinskii and Moriya have predicted strain-induced piezomagnetism in the antiferromagnetic rutile materials (43, 44), consistent with our observations. The secondary components, perpendicular to the magnetic moment orientation, clearly display the magnetic octupolar symmetry with a zero integrated magnetic moment, further illustrating their altermagnetic nature. Therefore, the calculation results suggest the coexistence of altermagnetism and weak-ferromagnetism in strained RuO₂ films.

In contrast, for the relaxed 17 nm film (lower panels of Fig 3A), as the temperature decreases, $I_{\text{SHG}}^{\text{SS}}(\varphi)$, demonstrating pure $4/mmm$ EQ contribution, shows an enhancement of its amplitude without any notable change in the anisotropy pattern. We note that no discernible change was observed in $I_{\text{SHG}}^{\text{PP}}$ (Fig. S11). Fig. 3C displays the temperature-dependent EQ SHG susceptibility tensor $\chi_{\text{SS}}^{\text{EQ}}$ (red circles) proportional to the square root of $I_{\text{SHG}}^{\text{SS}}$ at $\varphi = 45^\circ$. $\chi_{\text{SS}}^{\text{EQ}}$ exhibits a significant enhancement with an onset around 510 K, indicating the presence of an order parameter. To rule out a possible structural phase transition near T_c , we conducted temperature-dependent XRD measurements for the same 17 nm RuO₂ film, demonstrating a linear thermal expansion only of the out-of-plane lattice between 300 and 560 K (Fig. 3G). In-situ temperature-dependent reflection high-energy electron diffraction further supports no measurable changes in the in-plane structure (Fig. S12). We also show in Fig. 3C the temperature-independent $\chi_{\text{PP}}^{\text{EQ}}$ (white circles) and linear

reflectivity $R^{1\omega}$ (grey rectangles), verifying that the significant enhancement of χ_{SS}^{EQ} (red circles) originates from polarization-selective SHG response. We therefore attribute this observation to time-reversal symmetry breaking due to altermagnetism. Recent studies about RuO₂ suggested the point group symmetry $4'/mmm'$ at $T < T_c$ (1, 7, 25, 26), consistent with an altermagnetic configuration with moments along [001]. Because the anisotropy patterns in $I_{SHG}^{SS}(\varphi)$ appear the same with varying temperatures, we attribute the enhancement of I_{SHG}^{SS} below T_c to the i -type EQ SHG under $4'/mmm'$, thus distinct from the case of strained RuO₂ thin films. Consequently, while our SHG data on the 17 nm RuO₂ film cannot unambiguously determine the magnetic point group, our SHG results present evidence of a magnetic point group inherited from $4/mmm$ consistent with the $4'/mmm'$ group discussed in other works (1, 7, 25, 26), suggesting the existence of the altermagnetic phase transition and magnetic octupole order parameter below T_c in relaxed RuO₂ films.

Since the magnetic transition is proposed to be a Fermi surface instability of bulk RuO₂ (7), it is crucial to investigate how the electrical characteristics change, while maintaining magnetism as t decreases. Temperature-dependent electrical resistivity of RuO₂ shows that the metallic behavior of RuO₂ film is well preserved until 2 nm, whereas the 1.5 nm RuO₂ film shows clear insulating behavior (Fig. S13). The robust Drude response observed by optical spectroscopic ellipsometry further supports the metallicity of 2 nm RuO₂ (Fig. S14). To summarize these findings, we construct a temperature-thickness phase diagram revealing the various structural, electronic, and magnetic phases of RuO₂ films in Fig. 4. These suggest the presence of the novel altermagnetic- $mm2$ (polar) metallic phase in 2 nm RuO₂ film, uncovering the intriguing multifunctionality of the RuO₂ epitaxial heterostructure. Importantly, the various electronic/structural phases that exist below the magnetic transition (but above room temperature) down to 1 nm thickness provide distinctive advantages of RuO₂ thin film for possible applications (see Table S2 for a summary of previous SHG studies).

In summary, our work reveals the fingerprints of the altermagnetic order parameter of epitaxial RuO₂ film in nonlinear optical response across structural, electronic, and altermagnetic phase transitions. Interestingly, a structural phase transition from the centrosymmetric $4/mmm$ group to the inversion-symmetry-broken $mm2$ group is realized by using a epitaxially-strained heterostructure, promoting a novel altermagnetic polar phase in strained RuO₂ film. Our multiple experimental observations and theoretical analyses uncover the versatile correlated electronic/magnetic/structural phases in this system. Our findings pave the way for further exploration and understanding of the intricate interplay between multiple correlated degrees of freedom in altermagnetic RuO₂ films. The observed altermagnetic order parameters and their dependence on crystal symmetry open new avenues for investigating unique phenomena and applications in the realm of oxide heterostructures and novel altermagnetic materials.

References

1. L. Šmejkal, J. Sinova, T. Jungwirth, Emerging Research Landscape of Altermagnetism. *Phys. Rev. X* **12**, 040501 (2022).
2. L. Šmejkal, J. Sinova, T. Jungwirth, Beyond Conventional Ferromagnetism and Antiferromagnetism: A Phase with Nonrelativistic Spin and Crystal Rotation Symmetry. *Phys. Rev. X* **12**, 031042 (2022).
3. S. Hayami, Y. Yanagi, H. Kusunose, Momentum-Dependent Spin Splitting by Collinear Antiferromagnetic Ordering. *J. Phys. Soc. Japan.* **88**, 123702 (2019).
4. L. Šmejkal, R. González-Hernández, T. Jungwirth, J. Sinova, Crystal time-reversal symmetry breaking and spontaneous Hall effect in collinear antiferromagnets. *Sci. Adv.* **6**, eaaz8809 (2020).
5. S. Bhowal, N. A. Spaldin, Ferroically Ordered Magnetic Octupoles in *d*-Wave Altermagnets. *Phys. Rev. X* **14**, 011019 (2024).
6. R. M. Fernandes, V. S. de Carvalho, T. Birol, R. G. Pereira, Topological transition from nodal to nodeless Zeeman splitting in altermagnets. *Phys. Rev. B* **109**, 024404 (2024).
7. K.-H. Ahn, A. Hariki, K.-W. Lee, J. Kuneš, Antiferromagnetism in RuO₂ as *d*-wave Pomeranchuk instability. *Phys. Rev. B* **99**, 184432 (2019).
8. P. A. McClarty, J. G. Rau, Landau theory of altermagnetism. *arXiv preprint arXiv:2308.04484*, (2023).
9. S.-W. Cheong, F.-T. Huang, Altermagnetism with non-collinear spins. *npj Quantum Mater.* **9**, 13 (2024).
10. Y. Guo *et al.*, Spin-split collinear antiferromagnets: A large-scale ab-initio study. *Mater. Today Phys.* **32**, 100991 (2023).
11. I. Turek, Altermagnetism and magnetic groups with pseudoscalar electron spin. *Phys. Rev. B* **106**, 094432 (2022).
12. I. I. Mazin, K. Koepf, M. D. Johannes, R. González-Hernández, L. Šmejkal, Prediction of unconventional magnetism in doped FeSb₂. *Proc. Natl. Acad. Sci. U.S.A.* **118**, e2108924118 (2021).
13. I. I. Mazin, Altermagnetism in MnTe: Origin, predicted manifestations, and routes to detwinning. *Phys. Rev. B* **107**, L100418 (2023).
14. Y. Yu, T. Shishidou, S. Sumita, M. Weinert, D. F. Agterberg, Spin-orbit enabled unconventional Stoner magnetism. *arXiv preprint arXiv:2310.00838*, (2023).
15. D. S. Antonenko, R. M. Fernandes, J. W. Venderbos, Mirror chern bands and weyl nodal loops in altermagnets. *arXiv preprint arXiv:2402.10201*, (2024).
16. O. Fedchenko *et al.*, Observation of time-reversal symmetry breaking in the band structure of altermagnetic RuO₂. *Sci. Adv.* **10**, eadj4883 (2024).
17. Z. Feng *et al.*, An anomalous Hall effect in altermagnetic ruthenium dioxide. *Nat. Electron.* **5**, 735-743 (2022).
18. J. Krempaský *et al.*, Altermagnetic lifting of Kramers spin degeneracy. *Nature* **626**, 517-522 (2024).
19. R. D. Gonzalez Betancourt *et al.*, Spontaneous Anomalous Hall Effect Arising from an Unconventional Compensated Magnetic Phase in a Semiconductor. *Phys. Rev. Lett.* **130**, 036702 (2023).
20. S. Lee *et al.*, Broken Kramers Degeneracy in Altermagnetic MnTe. *Phys. Rev. Lett.* **132**, 036702 (2024).
21. T. Osumi *et al.*, Observation of a giant band splitting in altermagnetic MnTe. *Phys. Rev. B* **109**, 115102 (2024).
22. S. Reimers *et al.*, Direct observation of altermagnetic band splitting in CrSb thin films. *Nat. Commun.* **15**, 2116 (2024).
23. Z. Lin *et al.*, Observation of giant spin splitting and d-wave spin texture in room temperature altermagnet RuO₂. *arXiv preprint arXiv:2402.04995*, (2024).
24. A. Smolyanyuk, I. I. Mazin, L. Garcia-Gassull, R. Valentí, Fragility of the magnetic order in the prototypical altermagnet RuO₂. *Phys. Rev. B* **109**, 134424 (2024).
25. T. Berlijn *et al.*, Itinerant Antiferromagnetism in RuO₂. *Phys. Rev. Lett.* **118**, 077201 (2017).

26. Z. H. Zhu *et al.*, Anomalous Antiferromagnetism in Metallic RuO₂ Determined by Resonant X-ray Scattering. *Phys. Rev. Lett.* **122**, 017202 (2019).
27. B. Z. Gregory *et al.*, Strain-induced orbital-energy shift in antiferromagnetic RuO₂ revealed by resonant elastic x-ray scattering. *Phys. Rev. B* **106**, 195135 (2022).
28. A. Bose *et al.*, Tilted spin current generated by the collinear antiferromagnet ruthenium dioxide. *Nat. Electron.* **5**, 267-274 (2022).
29. S. Karube *et al.*, Observation of Spin-Splitter Torque in Collinear Antiferromagnetic RuO₂. *Phys. Rev. Lett.* **129**, 137201 (2022).
30. H. Yan, X. Zhou, P. Qin, Z. Liu, Review on spin-split antiferromagnetic spintronics. *Appl. Phys. Lett.* **124**, (2024).
31. M. Fiebig, T. Lottermoser, D. Meier, M. Trassin, The evolution of multiferroics. *Nat. Rev. Mater.* **1**, 16046 (2016).
32. J. H. Haeni *et al.*, Room-temperature ferroelectricity in strained SrTiO₃. *Nature* **430**, 758-761 (2004).
33. S. G. Jeong, J. Y. Oh, L. Hao, J. Liu, W. S. Choi, Correlated Quantum Phenomena of Spin–Orbit Coupled Perovskite Oxide Heterostructures: Cases of SrRuO₃ and SrIrO₃ Based Artificial Superlattices. *Adv. Funct. Mater.* **33**, 2301770 (2023).
34. S. Nair *et al.*, Engineering metal oxidation using epitaxial strain. *Nat. Nanotechnol.* **18**, 1005-1011 (2023).
35. W. Nunn *et al.*, Solid-source metal–organic molecular beam epitaxy of epitaxial RuO₂. *APL Mater.* **9**, (2021).
36. L. Zhao *et al.*, Evidence of an odd-parity hidden order in a spin–orbit coupled correlated iridate. *Nat. Phys.* **12**, 32-36 (2016).
37. L. Zhao *et al.*, A global inversion-symmetry-broken phase inside the pseudogap region of YBa₂Cu₃O_y. *Nat. Phys.* **13**, 250-254 (2017).
38. Y. Ahn *et al.*, Electric quadrupole second-harmonic generation revealing dual magnetic orders in a magnetic Weyl semimetal. *Nat. Photon.* **18**, 26-31 (2024).
39. M. Fiebig, V. V. Pavlov, R. V. Pisarev, Second-harmonic generation as a tool for studying electronic and magnetic structures of crystals: review. *J. Opt. Soc. Am. B* **22**, 96-118 (2005).
40. J. P. Ruf *et al.*, Strain-stabilized superconductivity. *Nat. Commun.* **12**, 59 (2021).
41. A. K. Rajapitamahuni *et al.*, Thickness-dependent insulator-to-metal transition in epitaxial RuO₂ films. *arXiv preprint arXiv:2312.07869*, (2023).
42. M. Uchida, T. Nomoto, M. Musashi, R. Arita, M. Kawasaki, Superconductivity in Uniquely Strained RuO₂ Films. *Phys. Rev. Lett.* **125**, 147001 (2020).
43. I. Dzialoshinskii, The problem of piezomagnetism. *Sov. Phys. JETP* **6**, 621 (1958).
44. T. Moriya, Piezomagnetism in CoF₂. *J. Phys. Chem. Solids* **11**, 73-77 (1959).
45. X. Gonze *et al.*, The Abinitproject: Impact, environment and recent developments. *Comput. Phys. Commun.* **248**, 107042 (2020).
46. A. H. Romero *et al.*, ABINIT: Overview and focus on selected capabilities. *J. Chem. Phys.* **152**, 124102 (2020).
47. M. Torrent, F. Jollet, F. Bottin, G. Zérah, X. Gonze, Implementation of the projector augmented-wave method in the ABINIT code: Application to the study of iron under pressure. *Comput. Mater. Sci.* **42**, 337-351 (2008).
48. M. T. Czyżyk, G. A. Sawatzky, Local-density functional and on-site correlations: The electronic structure of La₂CuO₄ and LaCuO₃. *Phys. Rev. B* **49**, 14211-14228 (1994).
49. A. I. Liechtenstein, V. I. Anisimov, J. Zaanen, Density-functional theory and strong interactions: Orbital ordering in Mott-Hubbard insulators. *Phys. Rev. B* **52**, R5467-R5470 (1995).
50. K. Momma, F. Izumi, VESTA 3 for three-dimensional visualization of crystal, volumetric and morphology data. *J. Appl. Crystallogr.* **44**, 1272-1276 (2011).
51. I. A. Vladimir, F. Aryasetiawan, A. I. Liechtenstein, First-principles calculations of the electronic structure and spectra of strongly correlated systems: the LDA+ U method. *J. Condens. Matter Phys.* **9**, 767 (1997).

52. R. Birss. (John Wiley & Sons, Inc., New York, 1964).
53. V. Mizrahi, J. E. Sipe, Phenomenological treatment of surface second-harmonic generation. *J. Opt. Soc. Am. B* **5**, 660-667 (1988).
54. H. Jeong *et al.*, Thickness-dependent orbital hybridization in ultrathin SrRuO₃ epitaxial films. *Appl. Phys. Lett.* **115**, 092906 (2019).
55. S. G. Jeong, W. S. Choi, A. Y. Mohamed, D.-Y. Cho, Atomic and electronic structures of correlated SrRuO₃/SrTiO₃ superlattices. *J. Korean Phys. Soc.* **82**, 386-391 (2023).
56. A. P. Mackenzie *et al.*, Hall effect in the two-dimensional metal Sr₂RuO₄. *Phys. Rev. B* **54**, 7425-7429 (1996).
57. M. Fiebig, D. Fröhlich, B. B. Krichevstov, R. V. Pisarev, Second Harmonic Generation and Magnetic-Dipole-Electric-Dipole Interference in Antiferromagnetic Cr₂O₃. *Phys. Rev. Lett.* **73**, 2127-2130 (1994).
58. L. W. Finger, R. M. Hazen, Crystal structure and isothermal compression of Fe₂O₃, Cr₂O₃, and V₂O₃ to 50 kbars. *J. Appl. Phys.* **51**, 5362-5367 (1980).
59. A. Rohrbach, J. Hafner, G. Kresse, Ab initio study of the (0001) surfaces of hematite and chromia: Influence of strong electronic correlations. *Phys. Rev. B* **70**, 125426 (2004).
60. P. Vaqueiro, G. G. Sobany, A powder neutron diffraction study of the metallic ferromagnet Co₃Sn₂S₂. *Solid State Sci.* **11**, 513-518 (2009).
61. W. Schnelle *et al.*, Ferromagnetic ordering and half-metallic state of Sn₂Co₃S₂ with the shandite-type structure. *Phys. Rev. B* **88**, 144404 (2013).
62. M. A. Korotin, V. I. Anisimov, Electronic structure and antiferromagnetism in CaCuO₂ and Sr₂CuO₂Cl₂. *Mater. Lett.* **10**, 28-33 (1990).
63. D. Vaknin, S. K. Sinha, C. Stassis, L. L. Miller, D. C. Johnston, Antiferromagnetism in Sr₂CuO₂Cl₂. *Phys. Rev. B* **41**, 1926-1933 (1990).
64. A. d. I. Torre *et al.*, Mirror symmetry breaking in a model insulating cuprate. *Nat. Phys.* **17**, 777-781 (2021).
65. G. Lautenschläger *et al.*, Magnetic phase transitions of MnWO₄ studied by the use of neutron diffraction. *Phys. Rev. B* **48**, 6087-6098 (1993).
66. D. Meier *et al.*, Second harmonic generation on incommensurate structures: The case of multiferroic MnWO₄. *Phys. Rev. B* **82**, 155112 (2010).
67. M. Assis *et al.*, Bridging experiment and theory: Morphology, optical, electronic, and magnetic properties of MnWO₄. *Appl. Surf. Sci.* **600**, 154081 (2022).
68. S. Xu *et al.*, Magnetoelectric coupling in multiferroics probed by optical second harmonic generation. *Nat. Commun.* **14**, 2274 (2023).
69. H. Béa *et al.*, Investigation on the origin of the magnetic moment of BiFeO₃ thin films by advanced x-ray characterizations. *Phys. Rev. B* **74**, 020101 (2006).
70. H. L. H'Mök *et al.*, Theoretical justification of stable ferromagnetism in ferroelectric BiFeO₃ by first-principles. *Comput. Mater. Sci.* **164**, 66-73 (2019).
71. Z. Sun *et al.*, Giant nonreciprocal second-harmonic generation from antiferromagnetic bilayer CrI₃. *Nature* **572**, 497-501 (2019).
72. J. F. Dillon, Jr., C. E. Olson, Magnetization, Resonance, and Optical Properties of the Ferromagnet CrI₃. *J. Appl. Phys.* **36**, 1259-1260 (1965).
73. S. Ghosh, N. Stojić, N. Binggeli, Structural and magnetic response of CrI₃ monolayer to electric field. *Physica B: Condensed Matter* **570**, 166-171 (2019).
74. H. Ju *et al.*, Possible Persistence of Multiferroic Order down to Bilayer Limit of van der Waals Material NiI₂. *Nano Lett.* **21**, 5126-5132 (2021).
75. Q. Song *et al.*, Evidence for a single-layer van der Waals multiferroic. *Nature* **602**, 601-605 (2022).
76. S. R. Kuindersma, J. P. Sanchez, C. Haas, Magnetic and structural investigations on NiI₂ and CoI₂. *Physica B+C* **111**, 231-248 (1981).
77. Y. Wang *et al.*, Switchable half-metallicity in A-type antiferromagnetic NiI₂ bilayer coupled with ferroelectric In₂Se₃. *npj comput. mater.* **8**, 218 (2022).
78. Z. Ni *et al.*, Imaging the Néel vector switching in the monolayer antiferromagnet MnPSe₃ with

- strain-controlled Ising order. *Nat. Nanotechnol.* **16**, 782-787 (2021).
79. K. Kurosawa, S. Saito, Y. Yamaguchi, Neutron Diffraction Study on MnPS₃ and FePS₃. *J. Phys. Soc. Japan.* **52**, 3919-3926 (1983).
 80. J. Yang, Y. Zhou, Q. Guo, Y. Dedkov, E. Voloshina, Electronic, magnetic and optical properties of MnPX₃ (X = S, Se) monolayers with and without chalcogen defects: a first-principles study. *RSC Advances* **10**, 851-864 (2020).
 81. H. Chu *et al.*, Linear Magnetoelectric Phase in Ultrathin MnPS₃ Probed by Optical Second Harmonic Generation. *Phys. Rev. Lett.* **124**, 027601 (2020).
 82. S. Calder, A. V. Haglund, A. I. Kolesnikov, D. Mandrus, Magnetic exchange interactions in the van der Waals layered antiferromagnet MnP₃. *Phys. Rev. B* **103**, 024414 (2021).

Acknowledgments

Funding: Structural characterization, transport, and ellipsometry at the University of Minnesota (UMN) were supported by the Air Force Office of Scientific Research (AFOSR) through Grant No. FA9550-21-1-0025 and FA9550-21-0460. Film synthesis (S.G.J and B.J.) was supported by the U.S. Department of Energy through grant numbers DE-SC0020211, and DE-SC0024710. S.N. was supported partially by the UMN Materials Research Science and Engineering Center (MRSEC) program under Award No. DMR-2011401. Film growth was performed using instrumentation funded by AFOSR DURIP awards FA9550-18-1-0294 and FA9550-23-1-0085. L.B. and T.B. are supported by the Air Force Office of Scientific Research under Award No. FA9550-21-1-0208. Parts of this work were carried out at the Characterization Facility at UMN which receives partial support from the National Science Foundation (NSF) through the MRSEC program under Award No. DMR-2011401. L.Z. acknowledges the support from the Air Force Office of Scientific Research (AFOSR) Young Investigator Program (YIP) grant no. FA9550-21-1-0065 and NSF MRSEC DMR-2309029. Electron microscopy work was performed at the Canadian Centre for Electron Microscopy a core research facility at McMaster University (also supported by NSERC (Natural Sciences and Engineering Research Council of Canada) and the Canada Foundation for Innovation). B.P. and N.B. were supported by AFOSR Grant No. FA9550-23-1-0275 for electron microscopy research. A.S. acknowledges the support of NSF Grant No. DMR-2104296. R.M.F. was supported by the AFOSR under Award No. FA9550-21-1-0423. This work was supported by the National Research Foundation of Korea (NRF) grant funded by the Korea government (MSIT) (No. 2022R1A2C2007847 (I.H.C, J.S.L), 2022M3H4A1A04074153, 2021R1A2C2011340 (W.S.C.), and RS-2023-00220471 (W.S.C.)).

Author contributions: S.G.J., I.H.C., J.S.L., and B.J. conceived the idea and designed the experiments. S.G.J. and S.N. grew the films by hybrid MBE under the supervision of B.J. S.G.J. characterized the films with reflection high-energy electron diffraction, atomic force microscopy, ellipsometry, and XRD. S.G.J. performed temperature-dependent XRD measurement and analysis. SHG with symmetry analysis was performed by I.H.C. under the supervision of J.S.L. and in discussion with L.Z. S.G.J., I.H.C., R.M.F., T.B., L.Z., J.S.L., and B.J. participated in the SHG analysis. DFT calculation was performed by L.B. under the direction of T.B. Group theory analysis was performed by L.B., T.B., and R.M.F. STEM measurement and analyses were performed by B.P. under the supervision of N.B. J.Y.O. performed X-ray absorption spectroscopy and ellipsometry under the supervision of W.S.C.

X-ray absorption and optical spectra analyses were performed by S.G.J. with the input of W.S.C. and A.S. S.G.J. and S.N. performed electric transport measurements under the supervision of B.J. S.G.J., I.H.C., J.S.L., and B.J. drafted the manuscript initially and revised it based on input and feedback from all the authors. S.G.J. and B.J. organized the different aspects of the project. J.S.L. and B.J. directed all aspects of the project.

Competing interests: Authors declare that they have no competing interests.

Data and materials availability: All data needed to evaluate the conclusions in the paper are present in the paper and/or the Supplementary Materials.

Supplementary Materials

Methods

Supplementary Text S1 to S2

Figs. S1 to S15

Tables S1 to S2

References (45–82)

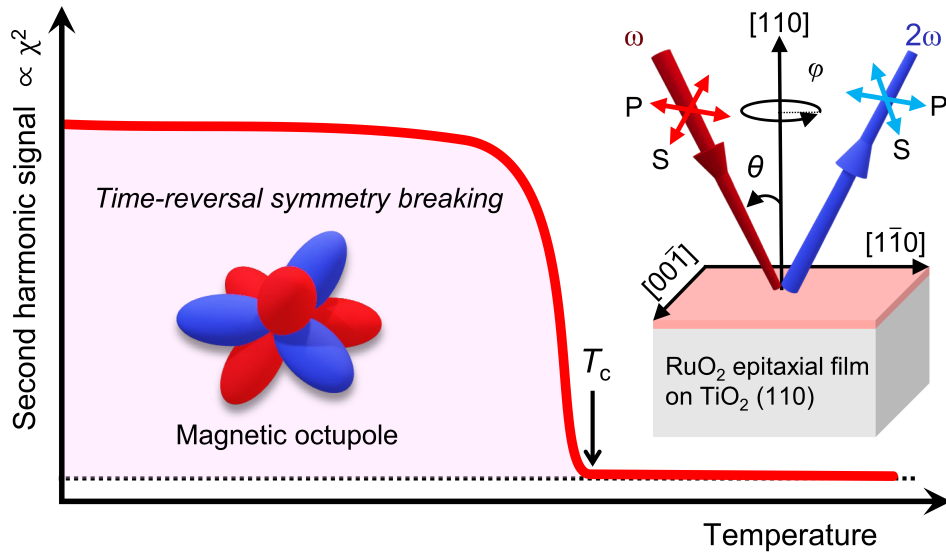


Fig. 1. Nonlinear optical second harmonic signal revealing altermagnetic order parameters in RuO₂ thin films. Schematic illustration of the second harmonic signal corresponding to the altermagnetic order parameter (magnetic octupole), which breaks time-reversal (TR) symmetry below the transition temperature T_c . The inset shows a schematic description of SHG geometry with polarization (S or P) of fundamental (ω , red) and SHG (2ω , blue) waves. SHG signal is proportional to the square of the nonlinear susceptibility χ .

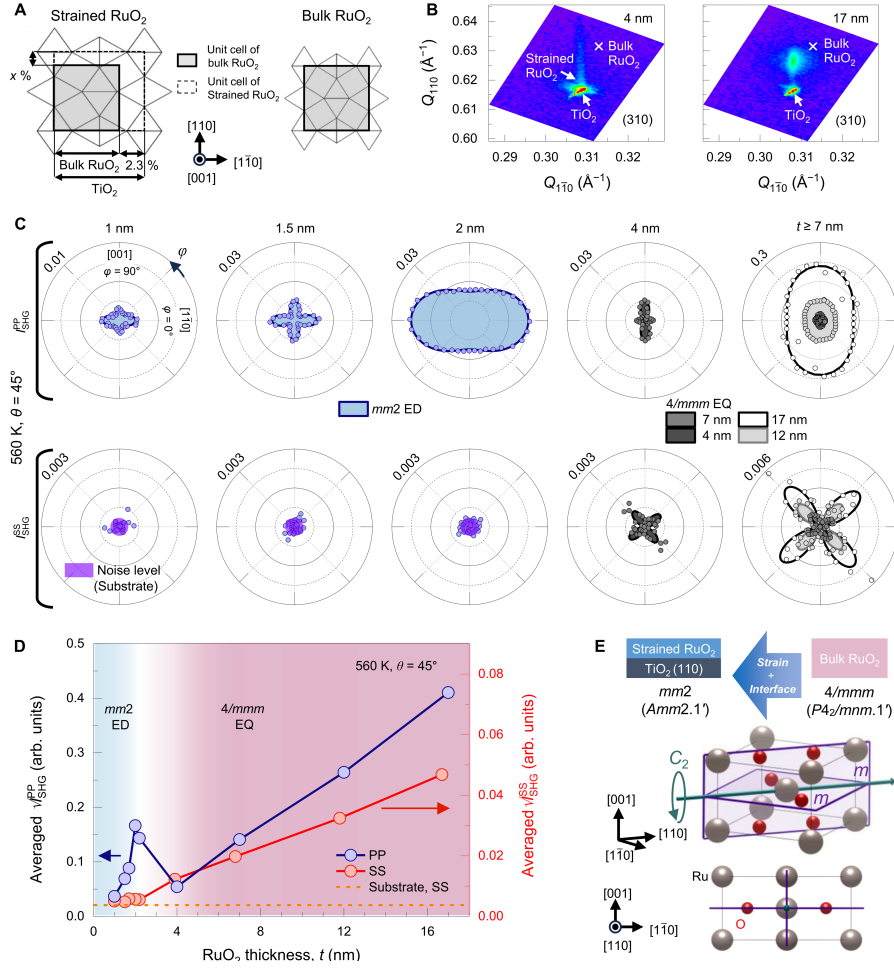


Fig. 2. Epitaxial strain induced crystal symmetry evolution of RuO₂/TiO₂ (110) films. Schematics of strain relations for RuO₂/TiO₂ (110) using bulk lattice values. $x\%$ is the lattice elongation along the [110] direction owing to the epitaxial strain. The grey square indicates the tetragonal unit cell of bulk $4/mmm$ RuO₂. **(B)** RSM XRD near (310) Bragg diffraction of TiO₂ for 4 and 17 nm RuO₂ films. **(C)** $I_{\text{SHG}}(\varphi)$ patterns with PP (upper panels) and SS polarization (lower panels) for RuO₂/TiO₂ (110) with different thickness t . The colored background and lines represent model fittings (details are in the main text). The noise level (purple) in $I_{\text{SHG}}^{\text{SS}}$ is estimated from the TiO₂ substrates. **(D)** t -dependent averaged $\sqrt{I_{\text{SHG}}}$ values for PP and SS polarizations at 560 K. The blue and red backgrounds represent regions where strained $mm2$ films (below 2 nm) and strain-relaxed $4/mmm$ (above 4 nm) are observed, respectively. **(E)** Conceptual illustration of structural phase transition from bulk RuO₂ to strained RuO₂/TiO₂ (110) thin films due to the combination of strain and interface effects. The bottom panel schematically shows two mirror planes (m) and a 2-fold rotation axis (C_2) for the rutile $mm2$ structure.

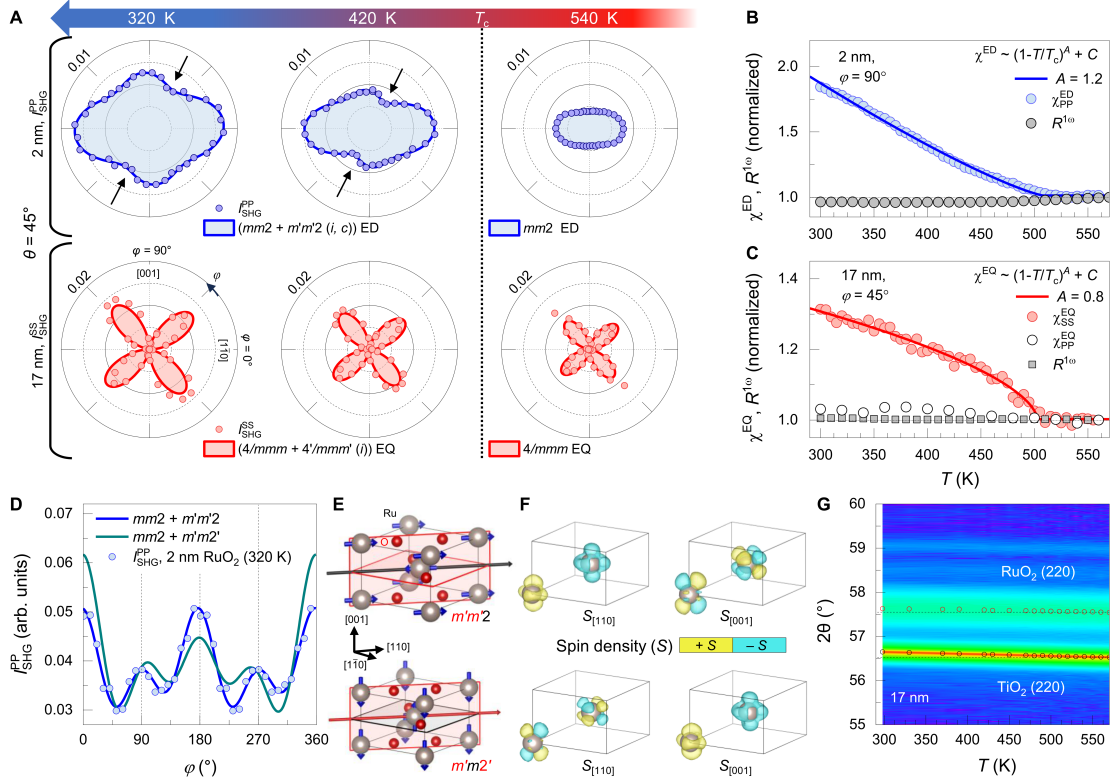


Fig. 3. Distinct magnetic order parameter for two different crystal symmetries of altermagnetic RuO₂ heterostructures. (A) $I_{\text{SHG}}(\varphi)$ pattern evolution for the 2 nm film with PP polarization (upper panels) and the 17 nm film with SS polarization (lower panels) for 320, 420, and 540 K. The arrows denote the appearance of two dips at $\varphi = 60^\circ$ and 240° below T_c . (B) Temperature-dependent normalized $\chi_{\text{PP}}^{\text{ED}}$ (blue) and $R^{1\omega}$ (grey) for 2 nm. (C) Temperature-dependent $\chi_{\text{PP}}^{\text{EQ}}$ (white), $\chi_{\text{SS}}^{\text{EQ}}$ (red), and $R^{1\omega}$ (grey), normalized by each value at 560 K for 17 nm. The solid lines are guides to the eye obtained from the phenomenological functional forms $(1 - T/T_c)^A + C$, where T , A , and C are the temperature, exponent parameter, and constant, respectively. (D) $I_{\text{SHG}}(\varphi)$ pattern for the 2 nm film at 320 K with two different symmetry considerations. The vertical dashed line indicates the directions perpendicular to the mirrors. (E) Schematics of the mirror planes and 2-fold rotation axis in the magnetic point group obtained from magnetic moments along $[110]$ ($m'm'2$, upper) and $[001]$ ($m'm'2'$, lower) cases. The antichronous rotation and/or mirror elements are marked with a prime and red color. (F) The calculated spin density of the $[110]$ ($S_{[110]}$, left) and $[001]$ components ($S_{[001]}$, right) for the $m'm'2$ (upper) and $m'm'2'$ (lower) cases. (G) Temperature-dependent θ - 2θ scans of XRD near (220) for the 17 nm film. The horizontal dashed line indicates the peak position at 550 K.

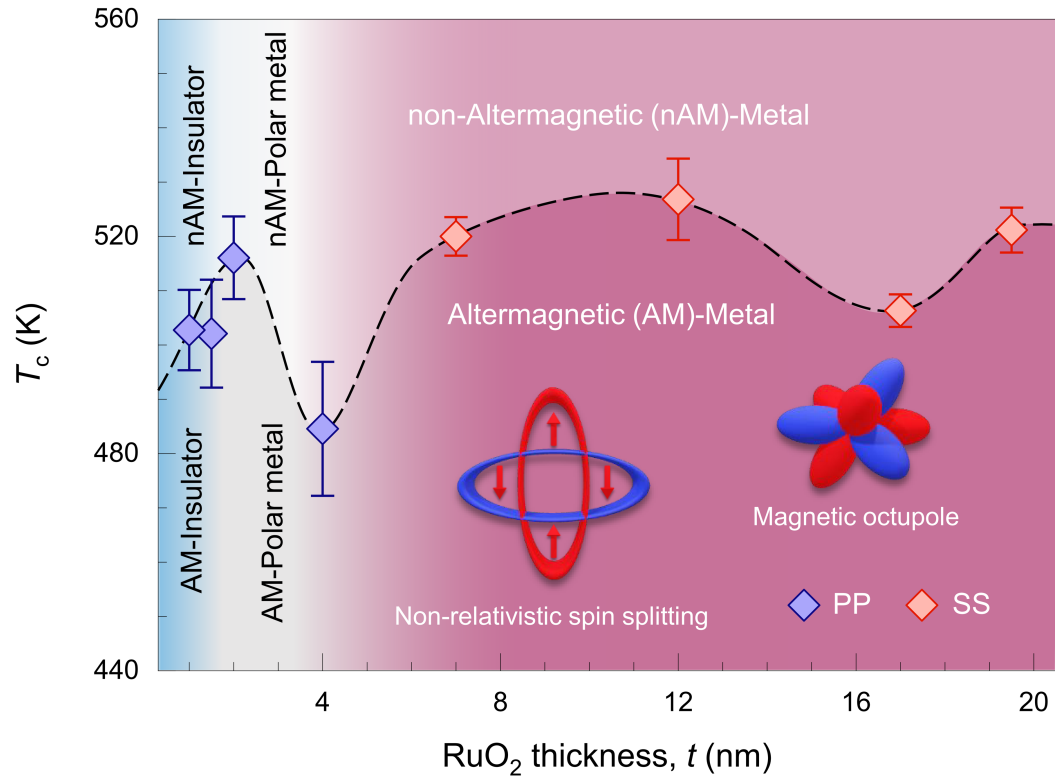


Fig. 4. The temperature-thickness phase diagram of altermagnetic RuO₂ heterostructures. The blue and red symbols were obtained from the PP and SS configurations of the SHG signals, respectively. The inset illustrates schematically the expected non-relativistic spin splitting and magnetic octupole order parameter (confirmed by the DFT calculation in Fig. 3F) in altermagnetic RuO₂. The blue (red) color indicates spin-up (down) polarization, denoted by the arrow directions.